Materials & Design 219 (2022) 110746

Contents lists available at ScienceDirect

Materials & Design

journal homepage: www.elsevier.com/locate/matdes

Martensitic transformation controlled by electromagnetic field: From experimental evidence to wireless actuator applications

Eneko Garaio [a,b], Paulo La Roca [a,b,c], Cristina Gómez-Polo [a,b], Vicente Sánchez-Alarcos [a,b], Vicente Recarte [a,b], José Ignacio Pérez-Landazábal [a,b,*]

[a] Institute for Advanced Materials and Mathematics (INAMAT^2), Universidad Pública de Navarra, Campus de Arrosadia, Pamplona 31006, Spain
[b] Department of Science, Universidad Pública de Navarra, Campus de Arrosadia, Pamplona 31006, Spain
[c] Centro Atómico Bariloche (CNEA), CONICET, S.C. de Bariloche 8400, Argentine

HIGHLIGHTS

- On Ni-Mn-In-Co-Cu shape memory alloy, the martensitic transformation can be externally induced by a low frequency electromagnetic field.
- Specific absorption rate determined by real-time dynamic magnetization measurements track the progress of the martensitic transformation.
- A strategy to achieve a remotely controllable battery-free wireless actuator is proposed based on the control of the austenite phase fraction.

GRAPHICAL ABSTRACT

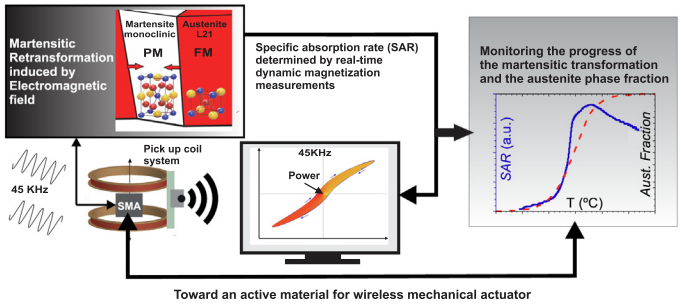

ARTICLE INFO

Article history:
Received 2 March 2022
Revised 21 April 2022
Accepted 9 May 2022
Available online 11 May 2022

Keywords:
Martensitic transformation
Electromagnetic field
Wireless
Battery-free
Actuator
SMA

ABSTRACT

Mechanical actuators based on shape memory alloys (SMA) are becoming a key component in the development of novel soft robotic applications and surgically implantable devices. Their working principle relies in the temperature induced martensitic transformation (MT), which is responsible of the actuation mechanism. In this work, we found experimental evidence to show that the martensitic transformation can be controlled by electromagnetic field (EF) by a wireless process in ferromagnetic shape memory alloys. It is shown that the martensitic transformation can be driven by an external EF (frequency 45 kHz) while the specific absorption rate (SAR), which was determined through real-time dynamic magnetization measurements, allows the instantaneous monitoring of the transformation evolution. On the basis of the obtained results, we propose a strategy to achieve a battery-free wireless SMA actuator that can be remotely controlled. This concept can be applicable to other SMA material that exhibit a similar magneto-structural phase transition.

1. Introduction

The development of new materials-actuators is a topic with an increasing interest in the scientific community, boosted by new advances in Soft Robotic and surgically implantable devices [1-4]. These technologies are vital for a wide range of applications, including manufacturing, manipulation, gripping, human–machine interaction, locomotion, artificial organs and muscles [5-8]. In this

* Corresponding author at: Institute for Advanced Materials and Mathematics (INAMAT2), Universidad Pública de Navarra, Campus de Arrosadia, Pamplona 31006, Spain.
E-mail addresses: paulo.laroca@unavarra.es, ipzlanda@unavarra.es (J. Ignacio Pérez-Landazábal).

https://doi.org/10.1016/j.matdes.2022.110746
0264-1275/

scope, an essential component is the "*soft actuator*" which can provide a deformable shape to the system and allows to interact it with the environment [2,9,10]. Shape Memory Alloys (SMA) are proposed as one of the most interesting "*soft actuator*" based materials [11,12]. The shape memory effect is the ability to regain shape during heating and is related to a first order non-diffusive phase transition (called martensitic transformation) between two different phases: the high temperature austenitic phase and the low temperature martensitic phase [13]. Comparing with other materials used as soft actuators, SMA have several advantages: they can undergo complex geometry changes, have the highest work per volume ratios, and can operate at relatively high frequencies (up to 100 Hz) [13,14]. Accordingly, many applications have been recently developed using SMA materials: soft robots with biologically locomotion and underwater displacement, sensing-actuation systems with high bladder voiding efficiency, a temperature-responsive device for gastrointestinal applications, a nano-fluidic pump for biochemical sampling and removable surgical clips [15-20].

However, the large work/volume ratio displayed by SMA implies a high-energy consumption and hence, it usually requires to employ batteries, which severely restricts their performance. This drawback becomes more important when developing small devices since conventional batteries usually do not contain the required energy in small volumes (i.e. low energy density) [21]. For this reason, electrochemical reactions or catalytic combustion of methanol were recently proposed to supply the high energy density required by SMA actuators [22,23]. In this sense, SMA controlled and powered by an external ~~A~~C magnetic field opens the door to the development of new battery-free wireless controllable SMA based actuators with a wide range of applications [24]. In addition, low frequency magnetic field can penetrate most materials, making this type of actuator promising for medical applications such as targeted drug delivery, microfluidics, and microsurgery [18-20].

Among SMA alloys, ferromagnetic shape memory alloys (FSMA) have been widely analysed in the last decades due to the possibility to take advantage of the magnetic changes in the alloy associated to the characteristic martensitic transformation. Particularly, in the so-called metamagnetic shape memory alloys, martensitic and austenitic phases have dissimilar magnetic properties, as it occurs in Ni-Mn-In based alloys where the low temperature paramagnetic (PM) monoclinic martensitic phase transforms to a ferromagnetic (FM) $L2_1$ austenitic phase [25,26].

Regarding the response of a magnetic material under the action of an alternating magnetic field of frequency f, the energy absorbed during each period or cycle is given by the magnetic work, that is [27]:

$$W = -\mu_0 \oint_{cycle} M_t \cdot dH_{app} \tag{1}$$

where M_t is the dynamic magnetization of the material and H_{app} is the magnetic field corresponding to the externally applied alternating electromagnetic field. If M_t is defined as mass magnetization (i.e. magnetic moment per mass of material) W directly corresponds to the energy mass density absorbed in each cycle. Therefore, the cyclically absorbed energy is proportional to the area enclosed into the hysteresis loop. Thermodynamically, the energy absorbed in each cycle would be employed in i) increase the material temperature and ii) carrying out the phase transitions, if any. Usually, the power mass density absorbed by a material from an electromagnetic field is defined as Specific Absorption Rate (*SAR*). Since W is the energy density absorbed in each cycle, from Equation (1) the *SAR* results in:

$$SAR = -f\mu_0 \oint_{cycle} M_t \cdot dH_{app} \tag{2}$$

In an electrically conductive FSMA, there are two mechanisms that contribute to Equation (2) leading to power absorption from a low frequency (LF) electromagnetic field: magnetic losses and eddy currents (also called Foucault's currents). Magnetic losses are triggered by any magnetic process that delays the dynamic magnetization M_t (e.g. magnetic anisotropy or domain wall rearrangement) and hence, the SAR arising from magnetic losses are proportional to the magnetization. The eddy currents, on the contrary, are caused by the electromotive force generated by the time varying magnetic field. If the material is electrically conductive, the electromotive force produces eddy currents and energy is absorbed by means of ohmic heating [28]. At LF electromagnetic frequencies, the energy absorbed by eddy current mechanism increases with the electrical conductivity and the magnetic permeability of the material. In addition, eddy currents are closely related to the geometry and they tend to disappear as the conductive FSMA sample gets smaller, because of the reduction of the magnetic flux crossing the sample. Hence, the *SAR* arising from eddy currents tends to be lower.

Heat generation involving the application of LF electromagnetic fields (magnetic induction heating) to advanced magnetic materials has been widely analysed in the literature on polymer curing, Magnetic Induction Swing Adsorption systems, controlled gas capture and release advanced synthesis procedures, among others [28-31]. Nevertheless, its application in the biomedical field employing magnetic nanoparticles (*magnetic hyperthermia*) has focused most of the scientific research in this field in recent years [32].

However, in spite of the extensive research on FSMAs, the analysis of the magnetic induction effects in these systems has been barely addressed. In these materials, the temperature increase induced by the externally applied alternate electromagnetic field would be an alternative procedure to induce the martensite to austenite transformation.

The present work propose the possibility to induce the martensitic transformation in a metamagnetic Ni-Mn-In-Co-Cu FSMA using a low radiofrequency electromagnetic field. The work describes a non-contact technology to deliver and monitor the required power to induce the transformation, while simultaneously enabling the tracking and control of the martensitic transformation evolution. The proposed device is completely battery-free in the sense that it gets all the required energy from an externally applied electromagnetic source. The approach presented here would increment the performance of battery-free wireless controllable SMA based actuators. Finally, the proposed technology, represents a starting point for future new materials designs in different applications fields ranging from medicine to robotics.

2. Experimental methods

A quinary Cu doped $Ni_{45}Mn_{35.5}In_{13.5}Co_4Cu_2$ alloy has been elaborated by arc-melting from pure elements. A small Cu quantity was added to obtain a lower thermal hysteresis [25,26]. The elaborated polycrystalline ingot was homogenized during 48 h at 800 °C and then quenched into iced water. Eventually, the geometry of the FSMA sample was quasi-spherical and its mass was 135 mg. It's important to note that all experiments described below were carried out on the same sample. Calorimetric characterization was carried out by differential scanning calorimeter (Q-1000 DSC, TA Instruments), by heating–cooling cycle performed at 10 °C/min. The measurement of the temperature dependence of magnetization was performed by SQUID magnetometry (QD MPMS XL-7)

between −10 °C and 60 °C at 2 K/min under 124 Oe. This intensity of the magnetic field (124Oe) was selected to match with the amplitude of the LF signal.

The temperature dependence of austenite fraction (f_A) was obtained from the DSC thermogram using the following equation: $f_A(T) = \frac{\int_{T1}^{T} \dot{Q}dT}{\int_{T1}^{T2} \dot{Q}dT}$, where T1 and T2 are temperatures corresponding to the DSC peak limits and $\dot{Q}$ is the heat flow.

Fig. 1a shows the schematic of the set up used for electromagnetic field application and *SAR* measurements [33]. The frequency of the field was 45 kHz whereas the intensity of the corresponding magnetic field was 10 kA.m^{-1}. By means of the pick-up coil system also described in the earlier cited work, the dynamic magnetization,M_t, of the FSMA sample was measured every 5 s after the magnetic field was switched on. Nevertheless, the signal originated from the applied magnetic field has to be subtracted. Therefore, an oppositely wounded compensation coil is used (see Fig. 1a). Then, the electromotive force (*emf*) induced in the coil system is measured when the SMA is in a) the pick-up coil and b) in compensation coil and afterwards, the subtraction is performed. In order to allow that sampling rate, a stepper motor placed the SMA actuator in the correct *z*-position relative to the pick-up and compensation coils.

From the so measured *emf*, the dynamic magnetization was obtained through fast Fourier transformation over 10 cycles and subsequent numerical integration, as described in the earlier cited work. Thereafter, the *SAR* values at each temperature and time were obtained by means of Equation (2) and its numerical integration. Finally, a commercial fiber optic thermometer measured the actual FSMA temperature *(Neoptix T1 sensor)*.

The estimations of the power absorbed by Eddy currents were made by means of cylindrical symmetry electromagnetic finite elements calculations. The following partial differential **Equation (3)** was solved assuming a spherical FSMA:

$$\Delta A_\phi + i\omega\sigma\mu A_\phi = 0 \tag{3}$$

where A_ϕ is the azimuthal component of the magnetic vector potential, σ and μ are the electrical conductivity and the magnetic permeability of the FSMA respectively, whereas ω is the angular frequency of the applied electromagnetic field. The computation domain was a spherical SMA located in the middle of a cylinder (see Fig. 1b). In order to include the externally applied magnetic field, H_z, fixed magnetic field boundary condition were applied. The radius of the assumed spherical FSMA material corresponds to the mass used during the experiments: 135 mg. The height and radius of the boundary cylinder was 25 and 12.5 times the radius of the sample, respectively.

3. Results and discussion

The dynamic magnetization,M_t (obtained from pick-up coils) under an electromagnetic field (Fig. 2, left), allows determining the Specific Absorption Rate (*SAR*) from the measured hysteresis loops (Fig. 2, right) [33]. In addition, the mechanisms leading to heat generation and hence to the phase transformation are both magnetic losses and eddy currents, contrary to previous works, in which eddy currents was the unique mechanism [34,35]. Therefore, the reduction of SMA size will not lead to a rapid reduction of SAR values and to a null absorbed heat.

Fig. 2b shows schematically the retransformation and shape recovery that taking place in the FSMA. The austenite (red) and different martensitic variants (white, yellow and blue) are drawn in the picture. The temperature increment, and the associated reverse MT are induced (above *Austenitic Start temperature, A_S*) by the externally applied LF electromagnetic field. In the present alloy, both martensite and austenite phases coexist at room temperature. As the temperature increases, the austenite becomes thermodynamically stable and hence martensite variants tend to disappear, giving rise to a macroscopic stress (σ) and a shape recovery effect (ε) that provides the *soft actuator* behavior required for the previously described applications [13]. Eventually, all the martensitic variants disappear above *Austenite Finish temperature*, resulting in a completely austenitic solid once the retransformation is fulfilled.

The calorimetric and magnetic characterization of Ni-Mn-In-Co-Cu FSMA is shown in Fig. 2c. The temperature dependence of the heat flow on heating (red) shows the typical endothermic peak related to the martensite to austenite transformation. The slope change at the Curie temperature Tc = 46 °C is related to the ferromagnetic–paramagnetic transition in austenite [36]. On the other side, the martensitic transformation shows a very small thermal hysteresis of 6–8 K, as shown in the low field (H = 124Oe) magnetization curve (blue) [26]. The magnetization curve presents a dramatic reduction above T_c associated with the ferro-paramagnetic transition.

The electrical conductivity of a Ni-Mn-In-Co-Cu FSMA also changes during the martensitic transformation. Variations up to %70 have been reported in similar Ni-Mn-In alloys in the literature, being the austenite more conductive than the martensite [37]. It can be inferred that the electrical conductivity at room temperature is roughly 2 MS.m^{-1} for austenitic (FM) phase whereas it decreases to around 1.2 MS.m^{-1} for the martensitic (PM) phase. With these conductivity values and the magnetic permeability deduced from magnetization in Fig. 2c ($\mu_r = 2.6$ for austenitic phase and $\mu_r = 3.5$ for martensitic phase), the power absorbed due to eddy currents was estimated to be: 0.8 W.g^{-1} and 0.6 W.g^{-1} for austenite and martensite phase, respectively.

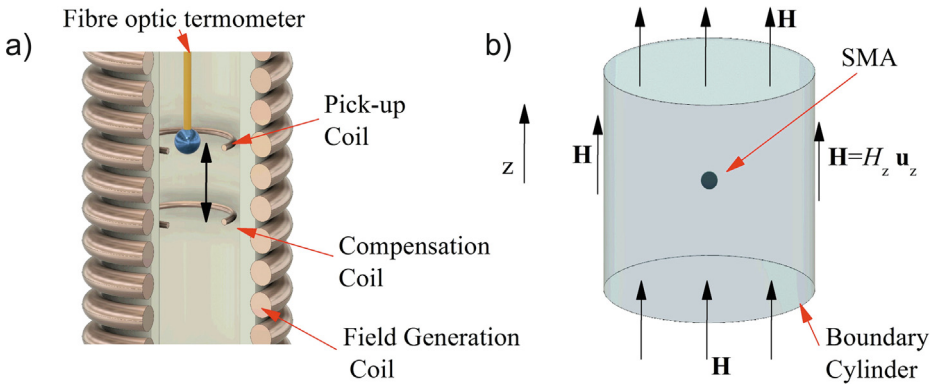

Fig. 1. a) Schematics of the setup used for electromagnetic field application and SAR measurements. b) Electromagnetic finite element scheme for eddy current calculations.

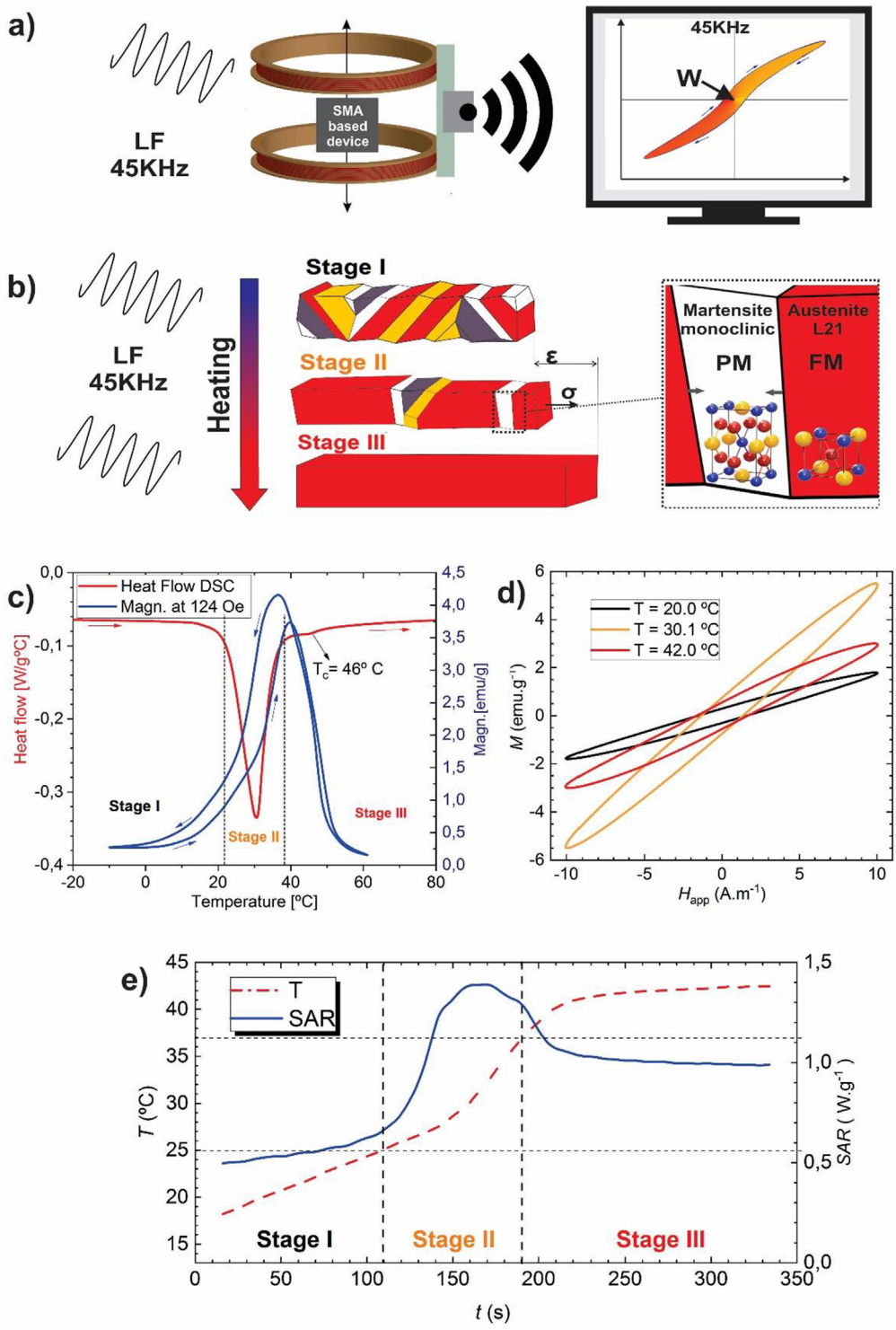

Fig. 2. a) Schematic representation of battery-free wireless procedure to monitor the required power to induce the transformation, the area enclosed inside the hysteresis loop corresponds to the magnetic work W absorbed by the material at each cycle. b) Schematic representation of martensitic transformation when heating the FSMA by LF. c) Magnetic and calorimetric characterization of Ni-Mn-In-Co-Cu alloy. d) Hysteresis loops measured at 45 kHz at three different temperatures form stages I, II and III. e) Time evolution of FSMA temperature and SAR (as measured from the hysteresis area in c).

To prove that the FSMA active material can work in a battery free wireless context, Fig. 2d shows the hysteresis-loops at different temperatures during electromagnetic induction heating process. The positive slope indicates that the material has a nonzero susceptibility and so, has magnetic losses. In addition, the area of the hysteresis-loop indicates that there is a positive *SAR* and hence an energy absorption (see Fig. 2a). Fig. 2e shows the time evolution of the *SAR* and mean temperature *T* under the application of the LF electromagnetic field. Both, the temperature increase and the positive *SAR* indicate that, indeed, there is and effective energy absorption. On the other hand, the measured *SARs* in Fig. 2e) are approximately 50 % larger than the ones estimated previously

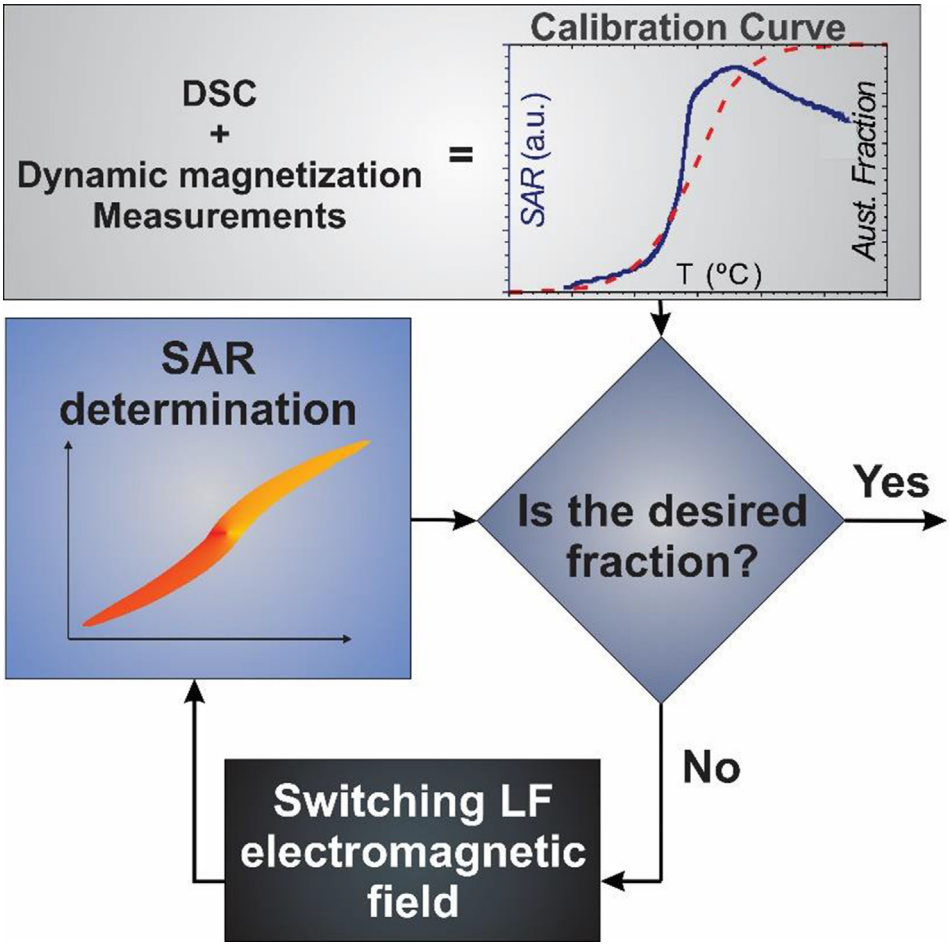

Fig. 4. Flow diagram reprinting the procedure to infer, control and asses the progression of martensitic transformation.

(0.8 W.g^{-1} for austenitic phase and 0.6 W.g^{-1}) by electromagnetic simulations, indicating that the energy adsorption is enhanced by the magnetic losses.

During the heating process, three stages can be distinguished, labeled I, II and III in Fig. 2b, 2c and 2e. At first stage (I), ranging from 18 to 25 °C, the FSMA has a coexistence of martensitic and austenitic phases and therefore it presents high electrical resistivity and low magnetization (see Fig. 2b). Consequently, the *SAR* is low since magnetic losses and eddy currents are not very effective in absorbing power. Nevertheless, it is important to remark that the absorbed power is enough to increment the temperature and reach the next stage.

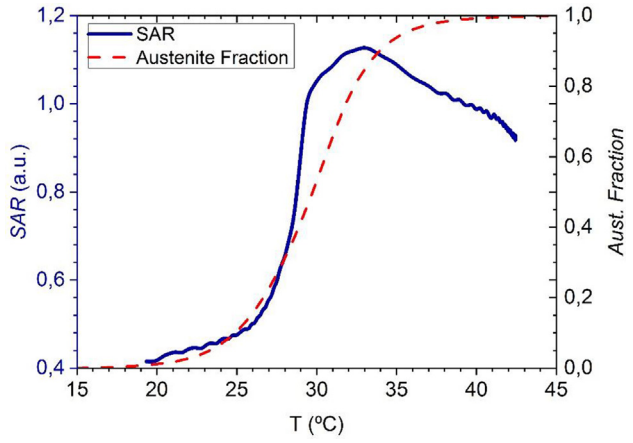

Fig. 3. SAR at different FSMA temperatures. The dashed line represents the corresponding austenitic fraction.

At second stage (II), ranging from 26 °C to 37 °C, the retransformation takes place and the austenitic phase fraction increases. Subsequently, the magnetization of the FSMA increases (see Fig. 2c and 2d) enhancing the power absorbed by magnetic losses and hence, incrementing the *SAR* (Fig. 2e). In addition, the electrical conductivity also increases as the austenitic fraction becomes more important and the eddy currents becomes larger, incrementing the SAR further. However, the temperature increment delays with respect to the *SAR* increment (see Fig. 2e). An important part of the absorbed power is employed in the martensite to austenite phase transition, not increasing the temperature. After approximately 30 s (see Fig. 2d), the temperature starts to increase abruptly. At this point, the martensitic fraction is drastically reduced, so less energy is required for the phase transformation and the absorbed power is mainly employed to increase the temperature.

Finally, at stage III, ranging from 38 °C to 43 °C, the martensitic transformation is almost completed. However, the temperature no longer rises above 43 °C and reaches a plateau (Fig. 2e). There are two main reasons for this plateau. First, the experimental set-up is not adiabatic and so heat dissipation increases with temperature and finally compensates the absorbed heat. Secondly, the magnetization decreases abruptly near the Curie temperature (T_c in Fig. 2c). Therefore, the magnetic losses are much less efficient. Neverthe-

less, the *SAR* are still high (about 80% of the maximum in Fig. 2e). Thus, eddy-currents would mainly contribute to the *SAR* increase in this stage. It is important to note that the FM-PM transition of austenite imposes a limit on the ability of the material to heat up, as a self-regulated process, so it can be an advantage for surgically implantation devices.

Therefore, the FSMA undergoes a retransformation (martensite to austenite) induced by the externally applied electromagnetic field. Fig. 3 shows the *SAR* and austenitic fraction at different temperatures (obtained from the heat flow on DSC measurements, see Experimental methods). This calibration curve allows a correlation between SAR and austenite phase fraction and enables monitoring the martensitic transformation progress by a wireless non-contact procedure. Besides, the SAR is a direct measurement of the required power to induce the transformation.

The scheme shown in Fig. 4 is a flow diagram representing the procedure to induce, control and assess the progression of the martensitic transformation for any potential actuator. This concept is the first step to develop a battery-free wireless controllable actuators based on magnetic SMA and can be applicable to any magnetic material that exhibit a similar magnetic phase transition [38-40].

4. Conclusions

In conclusion, the present work shows that the martensitic transformation can be induced by an external electromagnetic field in a Ni-Mn-In-Co-Cu shape memory alloy, being the magnetic losses and eddy currents responsible for the energy absorption process. An efficient pick-up coil that surrounds the active material would acquire the magnetic response before converting to SAR. The SAR directly monitors the required power to induce the transformation. Besides, the SAR allows monitoring the progress of the martensitic transformation and can be remotely controlled switching the external electromagnetic field. Therefore, the FSMA alloy (together with the described procedure) is proposed as a battery-free wireless and controllable active material for future potential mechanical actuators. The proposed technology, represents a starting point for future new materials designs in different applications fields ranging from medicine to robotics.

Declaration of Competing Interest

The authors declare that they have no known competing financial interests or personal relationships that could have appeared to influence the work reported in this paper.

Acknowledgments

This work has been carried out with the financial support of the Spanish "Agencia Estatal de Investigación (AEI), Ministerio de Ciencia, Innovación y Universidades" (Projects number RTI2018-094683-B-C54 (MCIU/AEI/FEDER, EU)), Navarra Government (Project number PC017-018 AMELEC). P. La Roca has received funding from "la Caixa" and "Caja Navarra" Foundations, under agreement LCF/PR/PR13/51080004.

References

[1] B. Grossi, H. Palza, J.C. Zagal, C. Falcón, G. During, Metarpillar: Soft robotic locomotion based on buckling-driven elastomeric metamaterials, Mater. Des. 212 (2021), https://doi.org/10.1016/j.matdes.2021.110285 110285.
[2] N. El-Atab, R.B. Mishra, F. Al-Modaf, L. Joharji, A.A. Alsharif, H. Alamoudi, M. Diaz, N. Qaiser, M.M. Hussain, Soft Actuators for Soft Robotic Applications: A Review, Adv. Intell. Syst. 2 (2020) 2000128, https://doi.org/10.1002/aisy.202000128.
[3] Joseph D Bronzino, Donald R Peterson, The biomedical engineering handbook, 2nd Editio, CRC Press, Springer, Boca Raton, n.d.
[4] F.A. Hassani, G.G.L. Gammad, R.P. Mogan, T.K. Ng, T.L.C. Kuo, L.G. Ng, P. Luu, N. V. Thakor, S.-C. Yen, C. Lee, Design and Anchorage Dependence of Shape Memory Alloy Actuators on Enhanced Voiding of a Bladder, Adv. Mater. Technol. 3 (2018) 1700184, https://doi.org/10.1002/admt.201700184.
[5] A. Zolfagharian, A. Kaynak, A. Kouzani, Closed-loop 4D-printed soft robots, Mater. Des. 188 (2020), https://doi.org/10.1016/j.matdes.2019.108411 108411.
[6] S. Chen, Y. Cao, M. Sarparast, H. Yuan, L. Dong, X. Tan, C. Cao, Soft Crawling Robots: Design, Actuation, and Locomotion, Adv. Mater. Technol. 5 (2020) 1900837, https://doi.org/10.1002/admt.201900837.
[7] H.-T. Lee, F. Seichepine, G.-Z. Yang, Microtentacle Actuators Based on Shape Memory Alloy Smart Soft Composite, Adv. Funct. Mater. 30 (2020) 2002510, https://doi.org/10.1002/adfm.202002510.
[8] A.K. Bastola, M. Hossain, The shape – morphing performance of magnetoactive soft materials, Mater. Des. 211 (2021), https://doi.org/10.1016/j.matdes.2021.110172 110172.
[9] L. Ding, N. Dai, X. Mu, S. Xie, X. Fan, D. Li, X. Cheng, Design of soft multi-material pneumatic actuators based on principal strain field, Mater. Des. 182 (2019), https://doi.org/10.1016/j.matdes.2019.108000 108000.
[10] S.I.H. Shah, S. Lim, Review on recent origami inspired antennas from microwave to terahertz regime, Mater. Des. 198 (2021), https://doi.org/10.1016/j.matdes.2020.109345 109345.
[11] J. Mohd Jani, M. Leary, A. Subic, M.A. Gibson, A review of shape memory alloy research, applications and opportunities, Mater. Des. 56 (2014) 1078–1113, https://doi.org/10.1016/j.matdes.2013.11.084.
[12] D. Rus, M.T. Tolley, Design, fabrication and control of soft robots, Nature. 521 (2015) 467–475, https://doi.org/10.1038/nature14543.
[13] K. Otsuka, C.M. Wayman, Shape memory materials, Cambridge University Press, Cambridge, 1999.
[14] P. Krulevitch, A.P. Lee, P.B. Ramsey, J.C. Trevino, J. Hamilton, M.A. Northrup, Thin film shape memory alloy microactuators, J. Microelectromechanical Syst. 5 (1996) 270–282, https://doi.org/10.1109/84.546407.
[15] X. Huang, K. Kumar, M.K. Jawed, A.M. Nasab, Z. Ye, W. Shan, C. Majidi, Chasing biomimetic locomotion speeds: Creating untethered soft robots with shape memory alloy actuators, Sci. Robot. 3 (2018) 1–4, https://doi.org/10.1126/scirobotics.aau7557.
[16] C.C. Ulloa, S. Terrile, A. Barrientos, Soft underwater robot actuated by shape-memory alloys "jellyrobcib" for path tracking through fuzzy visual control, Appl. Sci. 10 (2020) 1–22, https://doi.org/10.3390/app10207160.
[17] F. Arab Hassani, H. Jin, T. Yokota, T. Someya, N.V. Thakor, Soft sensors for a sensing-actuation system with high bladder voiding efficiency, Sci. Adv. 6 (2020) 2–10, https://doi.org/10.1126/sciadv.aba0412.
[18] S. Babaee, S. Pajovic, A.R. Kirtane, J. Shi, E. Caffarel-Salvador, K. Hess, J.E. Collins, S. Tamang, A.V. Wahane, A.M. Hayward, H. Mazdiyasni, R. Langer, G. Traverso, Temperature-responsive biometamaterials for gastrointestinal applications, Sci. Transl. Med. 11 (2019), https://doi.org/10.1126/scitranslmed.aau8581.
[19] R. Raman, E.B. Rousseau, M. Wade, A. Tong, M.J. Cotler, J. Kuang, A.A. Lugo, E. Zhang, A.M. Graybiel, F.M. White, R. Langer, M.J. Cima, Platform for micro-invasive membrane-free biochemical sampling of brain interstitial fluid, Sci. Adv. 6 (2020) eabb0657, https://doi.org/10.1126/sciadv.abb0657.
[20] E. Ryklina, A. Korotitskiy, I. Khmelevskaya, S. Prokoshkin, K. Polyakova, A. Kolobova, M. Soutorine, A. Chernov, Control of phase transformations and microstructure for optimum realization of one-way and two-way shape memory effects in removable surgical clips, Mater. Des. 136 (2017) 174–184, https://doi.org/10.1016/j.matdes.2017.09.024.
[21] V.H. Ebron, Z. Yang, D.J. Seyer, M.E. Kozlov, J. Oh, H. Xie, J. Razal, L.J. Hall, J.P. Ferraris, A.G. MacDiarmid, R.H. Baughman, Fuel-Powered Artificial Muscles, Science 311 (5767) (2006) 1580–1583.
[22] Q. Liu, W. Wang, M.F. Reynolds, M.C. Cao, M.Z. Miskin, T.A. Arias, D.A. Muller, P. L. McEuen, I. Cohen, Micrometer-sized electrically programmable shape-memory actuators for low-power microrobotics, Sci. Robot. 6 (2021), https://doi.org/10.1126/scirobotics.abe6663.
[23] T.R. L., L. Shuguang, Integrating chemical fuels and artificial muscles for untethered microrobots, Sci. Robot. 5 (2020) eabd7338. https://doi.org/10.1126/scirobotics.abd7338.
[24] M.-S. Kim, H.-T. Lee, S.-H. Ahn, Microrobots: Laser Controlled 65 Micrometer Long Microrobot Made of Ni-Ti Shape Memory Alloy (Adv. Mater. Technol. 12/2019), Adv. Mater. Technol. 4 (12) (2019) 1970064.
[25] Z. Li, J. Yang, D. Li, Z. Li, B. Yang, H. Yan, C.F. Sánchez-Valdés, J.L.S. Llamazares, Y. Zhang, C. Esling, X. Zhao, L. Zuo, Tuning the Reversible Magnetocaloric Effect in Ni–Mn–In-Based Alloys through Co and Cu Co-Doping, Adv. Electron. Mater. 5 (2019) 1800845, https://doi.org/10.1002/aelm.201800845.
[26] H. Le Yan, X.M. Huang, J.H. Yang, Y. Zhao, F. Fang, N. Jia, J. Bai, B. Yang, Z. Li, Y. Zhang, C. Esling, X. Zhao, L. Zuo, A strategy of optimizing magnetism and hysteresis simultaneously in Ni–Mn-based metamagnetic shape memory alloys, Intermetallics. 130 (2021), https://doi.org/10.1016/j.intermet.2020.107063 107063.
[27] J.A. Stratton, Electromagnetic Theory, McGraw-Hil, New York, 1941.
[28] R.P. Feynman, R.B. Leighton, M. Sands, Induced Currents, in: Feynman Lect. Phys., New millen, New York, 2010: p 21.
[29] M.M. Sadiq, H. Li, A.J. Hill, P. Falcaro, M.R. Hill, K. Suzuki, Magnetic Induction Swing Adsorption: An Energy Efficient Route to Porous Adsorbent Regeneration, Chem. Mater. 28 (2016) 6219–6226, https://doi.org/10.1021/acs.chemmater.6b02409.

[30] L. Melag, M.M. Sadiq, S.J.D. Smith, K. Konstas, K. Suzuki, M.R. Hill, Efficient delivery of oxygen via magnetic framework composites, J. Mater. Chem. A. 7 (2019) 3790–3796, https://doi.org/10.1039/c8ta07739h.
[31] C.W. Liu, C.Y. Qu, L. Han, D.Z. Wang, W.B. Xiao, X. Hou, Preparation of carbon fiber-reinforced polyimide composites via in situ induction heating, HIGH Perform. Polym. 29 (2017) 1027–1036, https://doi.org/10.1177/0954008316667789.
[32] E.A. Périgo, G. Hemery, O. Sandre, D. Ortega, E. Garaio, F. Plazaola, F.J. Teran, Fundamentals and advances in magnetic hyperthermia, Appl. Phys. Rev. 2 (4) (2015) 041302.
[33] E. Garaio, J.M. Collantes, F. Plazaola, J.A. Garcia, I. Castellanos-Rubio, A multifrequency eletromagnetic applicator with an integrated AC magnetometer for magnetic hyperthermia experiments, Meas. Sci. Technol. 25 (11) (2014) 115702.
[34] R.N. Saunders, J.G. Boyd, D.J. Hartl, J.K. Brown, F.T. Calkins, D.C. Lagoudas, A validated model for induction heating of shape memory alloy actuators, Smart Mater. Struct. 25 (2016) 45022, https://doi.org/10.1088/0964-1726/25/4/045022.
[35] A. Razek, S. Dufour, G. Vinsard, Induction heating of a shape memory alloy beam, EPJ Appl. Phys. 83 (2018) 1–6, https://doi.org/10.1051/epjap/2018170394.
[36] V. Sánchez-Alarcos, V. Recarte, J.I. Pérez-Landazábal, E. Cesari, J.A. Rodríguez-Velamazán, Long-range atomic order and entropy change at the martensitic transformation in a Ni-Mn-In-Co metamagnetic shape memory alloy, Entropy. 16 (2014) 2756–2767, https://doi.org/10.3390/e16052756.
[37] B. Zhang, X.X. Zhang, S.Y. Yu, J.L. Chen, Z.X. Cao, G.H. Wu, Giant magnetothermal conductivity in the Ni-Mn-In ferromagnetic shape memory alloys, Appl. Phys. Lett. 91 (2007) 89–92, https://doi.org/10.1063/1.2753710.
[38] H.-L. Yan, L.-D. Wang, H.-X. Liu, X.-M. Huang, N. Jia, Z.-B. Li, B. Yang, Y.-D. Zhang, C. Esling, X. Zhao, L. Zuo, Giant elastocaloric effect and exceptional mechanical properties in an all-d-metal Ni–Mn–Ti alloy: Experimental and ab-initio studies, Mater. Des. 184 (2019), https://doi.org/10.1016/j.matdes.2019.108180 108180.
[39] M. Zelený, P. Sedlák, O. Heczko, H. Seiner, P. Veřtát, M. Obata, T. Kotani, T. Oda, L. Straka, Effect of electron localization in theoretical design of Ni-Mn-Ga based magnetic shape memory alloys, Mater. Des. 209 (2021), https://doi.org/10.1016/j.matdes.2021.109917 109917.
[40] S. Samothrakitis, C.B. Larsen, R. Woracek, L. Heller, J. Kopeček, G. Gerstein, H.J. Maier, M. Rameš, M. Tovar, P. Šittner, S. Schmidt, M. Strobl, A multiscale study of hot-extruded CoNiGa ferromagnetic shape-memory alloys, Mater. Des. 196 (2020), https://doi.org/10.1016/j.matdes.2020.109118 109118.